PAPER

Check for updates

Fluorescent nanodiamond – hyaluronate conjugates for target-specific molecular imaging

Hye Hyeon Han, [a] Homan Kang, [b] Seong-Jong Kim, [a] Rahul Pal, [c] Anand T. N. Kumar, [c] Hak Soo Choi [b] and Sei Kwang Hahn [*a]

Despite wide investigation on molecular imaging contrast agents, there are still strong unmet medical needs to enhance their signal-to background ratio, brightness, photostability, and biocompatibility with multimodal imaging capability. Here, we assessed the feasibility of fluorescent nanodiamonds (FNDs) as carbon based photostable and biocompatible materials for molecular imaging applications. Because FNDs have negatively charged nitrogen vacancy (NV) centers, they can emit bright red light. FNDs were conjugated to hyaluronate (HA) for target-specific molecular imaging. HA is a biocompatible, biodegradable, and linear polysaccharide with abundant HA receptors in the liver, enabling liver targeted molecular imaging. *In vitro* cell viability tests revealed the biocompatibility of HA−FND conjugates and the competitive cellular uptake test confirmed their target-specific intracellular delivery to HepG2 cells with HA receptors. In addition, *in vivo* fluorescence lifetime (FLT) assessment revealed the imaging capability of FNDs and HA−FND conjugates. After that, we could confirm the statistically significant liver-targeted delivery of HA−FND conjugates by *in vivo* imaging system (IVIS) analysis and *ex vivo* biodistribution tests in various organs. The renal clearance test and histological analysis corroborated the *in vivo* biocompatibility and safety of HA−FND conjugates. All these results demonstrated the feasibility of HA−FND conjugates for further molecular imaging applications.

1. Introduction

A variety of molecular imaging agents have been developed for optical imaging such as fluorescence imaging, photoacoustic imaging, ultrasound imaging, magnetic resonance imaging (MRI), X-ray computed tomography (CT), and positron emission tomography (PET).[1-7] These advances have been enabled by the development of multifunctional photonic nanomaterials with brightness, biocompatibility, photostability, and high performance.[8] Currently, quantum dots,[9-11] gold nanoparticles,[12,13] iron oxide nanoparticles,[14] organic dyes,[15] fluorescent proteins,[16] carbon nanomaterials[17] and various nanomaterials are commonly used as molecular imaging contrast agents.[18] Despite all these great efforts, there are still unmet medical needs for multifunctional molecular imaging agents, especially for multimodal molecular imaging applications. For example, the combination of PET and MRI can provide greatly advantageous complementary data for accurate disease diagnosis by PET-guided MR imaging, *in vivo* quantification of smart MR probes, and cross-calibration and validation.

Recently, among various nanomaterials, nanodiamonds (NDs) have attracted huge attention due to their chemical stability, high affinity to biomolecules, biocompatibility, and facile surface modification. In addition, NDs have been appeared to be more biocompatible than other carbon materials and actively investigated for various diagnostic and therapeutic applications.[8,19-22] Fluorescent nanodiamonds (FNDs) contain negatively charged nitrogen vacancy (NV) centers, which are the point defects in the lattice of NDs. The NV center consists of a lattice vacancy and a nearest-neighbor pair of a nitrogen atom obtained by the thermal annealing in the formation process of FNDs.[23] NV centers are notable for their stable fluorescence as well as optically detectable electron spin resonance.[24] They absorb light strongly at the wavelength of 560 nm and emit fluorescence at 700 nm, acting as built-in fluorophores.[25] The highly bright FNDs have NV centers up to 3 ppm with the concentration of about 300 centers in a 100 nm ND. FNDs are photostable even in high-power excitation without photoblinking and photobleaching so FNDs can be used as a fluorescent imaging contrast agent.[26] However, NDs tend to individually aggregate in the physiological medium due to high surface activity and electrostatic interaction.[27] Accordingly, the surface of NDs has been modified to enhance the dispersibility and stability. In particular, FNDs have been

aDepartment of Materials Science and Engineering, Pohang University of Science and Technology (POSTECH), 77 Cheongam-ro, Nam-gu, Pohang, Gyeongbuk, KR 37673, Korea. E-mail: skhanb@postech.ac.kr; Fax: +82 54 279 2399; Tel: +82 54 279 2159

bGordon Center for Medical Imaging, Department of Radiology, Massachusetts General Hospital & Harvard Medical School, 149 13th Street, Boston, MA 02114, USA

cAthinoula A. Martinos Center for Biomedical Imaging, Massachusetts General Hospital & Harvard Medical School, 149 13th Street, Boston, MA 02114, USA

modified with polymers such as polyethylene glycol (PEG) for molecular imaging[28] and polyglycerol (PG) for drug delivery in cancer cells,[8,29] cell tracking,[25,30–32] and *in vivo* imaging.[33]

Here, we developed HA–FND conjugates by the amide bond formation between carboxylated FNDs and end-group aminated hyaluronate (HA) for target-specific molecular fluorescence imaging *via* HA receptor mediated endocytosis (Fig. 1). HA is a natural ubiquitous polysaccharide and free from safety concerns with excellent biocompatibility and biodegradability in the body.[34–37] There are several HA receptors in the body such as cluster determinant 44 (CD44), HA receptor for endocytosis (HARE), lymphatic vessel endothelial HA receptor-1 (LYVE-1), and receptor for hyaluronate-mediated motility (RHAMM).[38] In addition, CD44 receptors are overexpressed in various cancer cells.[39,40] Thus, HA has been widely used for the target-specific drug delivery to the liver and tumor tissues with abundant HA receptors.[41–43] To demonstrate the feasibility of HA–FND conjugates as a new molecular imaging agent, we conducted *in vitro* cell viability test, competitive cellular uptake tests, fluorescence lifetime (FLT) imaging, *in vivo* liver targeted IVIS imaging with histological analysis and the biodistribution tests. To our best knowledges, this is the first report on the liver targeted delivery of HA–FND conjugates.

2. Materials and methods

2.1. Materials

Fluorescent nanodiamonds (FNDs, carboxylated, 100 nm, 1 mg mL^{-1}) in DI water) were obtained from Adamas Nano (Raleigh, NC), sodium hyaluronate (HA, 200 kDa) from Lifecore Co. (Chaska, MN) and *N*-hydroxysulfosuccinimide (sulfo-NHS) from Georgiachem. 1,4-Diaminobutane (DAB) and sodium cyanoborohydride (NaBH3CN) were purchased from Sigma Aldrich (Seoul, Korea). 1-Ethyl-3-(3-dimethylaminopropyl) carbodiimide hydrochloride (EDC) and 5-aminofluorescein (FTIC) were purchased from Tokyo Chemical Industry (Tokyo, Japan). Dulbecco's modified Eagle's medium-high glucose (DMEM), fetal bovine serum (FBS), antibiotics, and phosphate buffered saline (PBS, pH 7.4) were obtained from Invitrogen (Carlsbad, CA). Cell counting kit-8 (CCK-8) was obtained from DoGenBio Co. Human liver epithelial cell line (FL83B), human liver cancer cell line (HepG2), adenocarcinomic human alveolar basal epithelial cells (A549) and human embryonic kidney 293 cells (HEK293) were purchased from Korean Cell Line Bank (Seoul, Korea). 6 week-old female balb/c nude mice were purchased at the Orient Bio (Seongnam, Korea). Alfalfa free feed (AIN-93G) for mouse was purchased from Saeronbio Co. (Uiwang, Korea). All animal
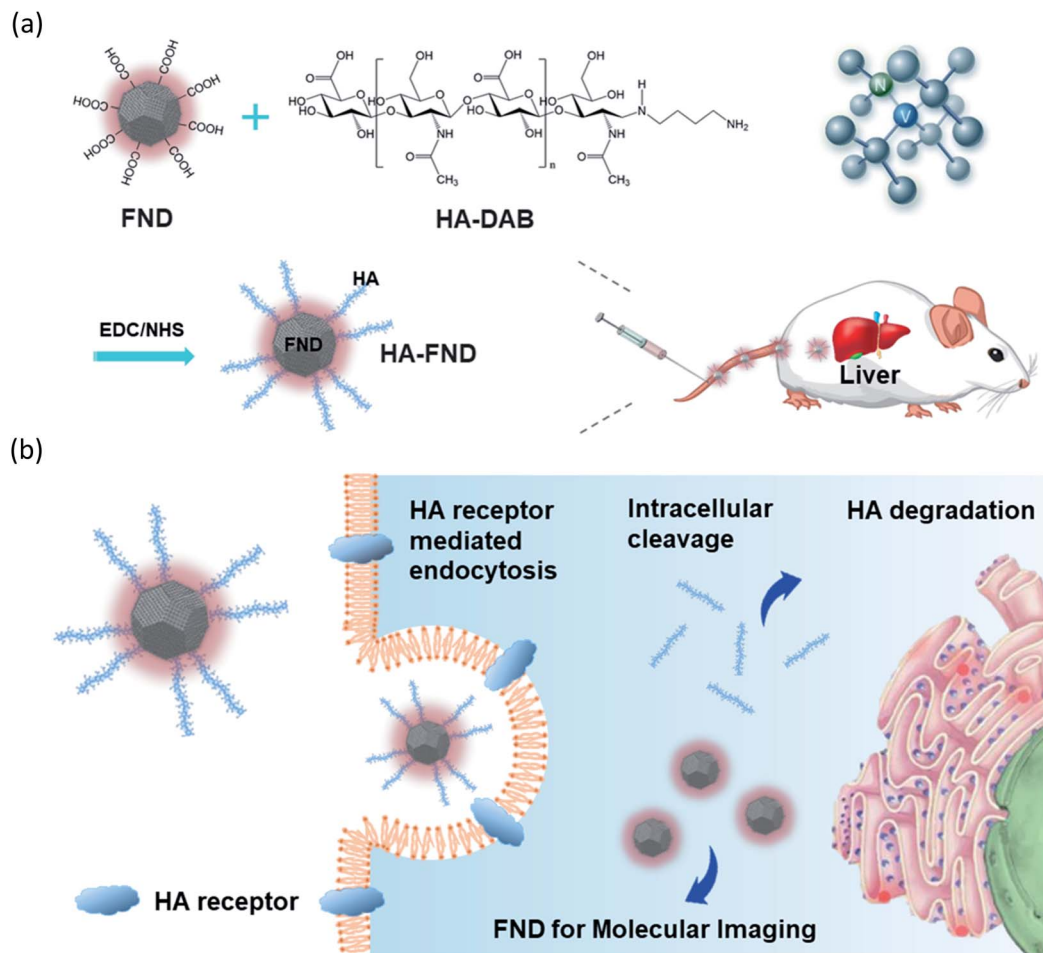
Fig. 1 Schematic illustration for (a) the synthesis of HA–FND conjugates and liver targeted delivery after intravenous injection, and (b) the target-specific delivery of HA–FND conjugates to liver cells *via* the HA receptor mediated endocytosis.

experiments followed the guidelines for Care and Use of Laboratory Animals of the Pohang University of Science and Technology (POSTECH) and approved by the Institutional Animal Care and Use Committee (IACUC).

2.2. Synthesis of diaminobutane-modified HA

HA (100 mg) was dissolved in sodium carbonate buffer (pH 9). DAB was added to the HA solution at a molar ratio of DAB to HA of 10. The pH of the mixed solution was changed to 8.5. $NaBH_3CN$ was added to the reaction mixture at a molar ratio of 5 and stirred in a 37 °C incubator for 3 days. After reaction, the solution was dialyzed (MWCO = 10 000) with 0.3 M NaCl solution for 2 days and DI water for a day, and lyophilized for 2 days.

HA–FITC–DAB was obtained by synthesizing of HA–DAB and FTIC.

2.3. Synthesis of HA–FND conjugates

HA–FND conjugates were synthesized by the addition of EDC (0.1 mg) and sulfo-NHS (0.1 mg) to the solution of FNDs (1 mg) with the activation of the carboxyl groups of FNDs for 1 h. After that, the solution was centrifuged at 5000 g and 25 °C for 15 min and the precipitate was dispersed in DI water. HA–DAB (0.1 mg) was added to the solution of FNDs and stirred for 12 h. Finally, the HA–FND conjugates were obtained by centrifugation and dispersed in DI water.

2.4. Characterization of HA–FND conjugates

HA–FND conjugates were analyzed by ^1H nuclear magnetic resonance (^1H NMR, DPX500, Bruker) and Fourier Transform – infrared spectroscopy (FT-IR Microscope, Cary 600, Agilent Technologies). The particle size distribution and zeta potential were measured with Zetasizer (MAN383-01, Malvern Instruments). The size and morphology of HA–FND conjugates were analyzed by high resolution transmission electron microscopy (HR-TEM) (JEM-2200FS, Jeol Ltd) at an operating voltage of 200 kV. The photo-images of FNDs and HA–FND conjugates (0.1 mg mL^{-1}) were obtained with a 532 nm laser and a 600 nm long band filter in a dark room. Fluorescent intensity and UV-vis absorption spectroscopy of FNDs and HA–FND conjugates were analyzed with a microplate fluorometer (Fluoroskan ascent FL, Thermo Scientific) and a UV spectrophotometer (JASCO J-715).

2.5. Cellular uptake assessment for targeted delivery

HepG2 and FL38b cells were seeded and incubated for 24 h on each eight chambers confocal slide at a density of 2×10^4 cells per well containing the high glucose DMEM with 10 vol% FBS and 1 vol% antibiotics. To check the cellular uptake of HA–FND conjugates *via* HA receptor mediated endocytosis, HepG2 cells were pre-incubated with 200 μL of HA (10 mg mL^{-1}) for 2 h and then with PBS as a control, FNDs, and HA–FND conjugates at a concentration of 20 μg mL^{-1}. After 2 h, the cells were washed with PBS (pH 7.4), fixed with 4% formaldehyde solution and stained with DAPI. Likewise, FL83b cells were treated with HA–FITC–FND conjugates (50 μg mL^{-1}) for 4 h, fixed, and stained with DAPI. The cellular uptake was visualized by confocal

microscopy (TCS SP5, Leica). In addition, HepG2, A549, and HEK293 cells were seeded on a 96-well plate at a density of 2×10^4 cells per well and incubated with PBS as a control, FNDs, and HA–FND conjugates at a concentration of 50 μg mL^{-1} in DMEM, respectively. After 12 h incubation, each cell was washed with PBS (pH 7.4) and the fluorescence intensity was quantified with a microplate fluorometer ($n = 3$).

2.6. *In vitro* biocompatibility of HA–FND conjugates

HepG2 and FL83b cells were cultured in DMEM supplemented with 10 vol% FBS and 1 vol% antibiotics in a humidified 5% CO_2 incubator at 37 °C. The cells were seeded in a 96-well plate at a density of 2×10^4 cells per well and treated with different concentrations of HA–FND conjugates from 0 to 1 mg mL^{-1}. After 24 h, the media were replaced with serum free media and CCK-8 agent, and the cells were incubated for 4 h. The absorbance was measured at 450 nm with a spectrophotometer (Microplate reader, SoftMax). This process was repeated for the cell viability tests for 7 days ($n = 3$).

2.7. Fluorescence lifetime imaging

Animals were housed in an AAALAC-certified facility and were studied under the supervision of MGH IACUC in accordance with the approved institutional protocol (2016N000136). Six-week-old CD-1 mice (male, 25–30 g) were purchased from Charles River Laboratories (Wilmington, MA). Mice were maintained under anesthesia with isoflurane and oxygen during the preparation prior to injection. *In vivo* FLT imaging was performed using a previously published custom-built time domain (TD) imaging system.[44] The small animal imaging system was consisted of a supercontinum laser and tunable filter (EXR-20, SuperK Varia, NKT Photonics, 80 MHz repetition rate; 400–850 nm tuning range) to provide 540 ± 20 nm excitation, a multimode fiber (Thorlabs; Newton, NJ) delivering light to the sample, and a gated intensified CCD (LaVision, Picostar, 500 V gain, 0.1 to 1 s integration time, 150 ps steps, 256 × 344 pixels after 4 × 4 hardware binning). The output of the optical fiber was delivered to the animal using a diffusing filter (ED1-S50-MD, Thorlabs), which provided 10–20 mW average total power across the illumination area (∼8 cm diameter). Time resolved fluorescence emission was collected in reflectance mode using a 580 nm long pass filter. Imaging was performed with a gate width of 500 ps and 150 ps steps for an acquisition time of 6.0 ns. Camera integration time for each step was between 100–600 ms.

2.8. Processing and data analysis of FLT imaging

Algorithms for the fluorescence image processing were implemented in MATLAB (Mathworks, Natick, MA). Fluorescence intensity data were generated from each FLT data set by adding the images over all the temporal gates. FLT map was obtained by plotting the data from individual pixels as delay *versus* log(counts) followed by fitting the decay portion of time domain fluorescence profiles at each pixel to a single exponential function of $e^{-t/\tau(r)}$, where r denotes pixel location and $\tau(r)$ constitutes a lifetime map.

2.9. *In vivo* molecular imaging with IVIS

For *in vivo* molecular imaging of FNDs and HA–FND conjugates, we used 6 week female balb/c nude mice (weight ≈ 20 g) for conducting all animal experiments with IVIS (Maestro 2, CRI). Alfalfa free diets were fed to mice for 7 days before imaging. The mice were anesthetized with a vaporized-isoflurane system (1 L min^{-1} of oxygen and 0.75% isoflurane) and located on the sample stand of IVIS. After taking images of the control, we intravenously injected FNDs and HA–FND conjugates (100 μL, 20 mg mL^{-1}) at the concentrations for the same fluorescence of FNDs and HA–FND conjugates. We observed the liver targeting for 7 days at an excitation wavelength of 605 nm and an emission wavelength of 680 nm ($n = 3$).

2.10. Biodistribution analysis

FNDs and HA–FND conjugates (100 μL, 10 mg mL^{-1} of total FNDs) were intravenously injected into 6 week female balb/c nude mice (weight ≈ 20 g). After 6 h and 30 h, the mice were fully anesthetized by intraperitoneal injection of the mixture of PBS (pH 7.4), ketamine and rompum (volume ratio = 200 : 40 : 10), and sacrificed by cervical dislocation. After that, the liver, heart, lung, kidney and spleen were dissected, fixed in 4% formaldehyde overnight, dried for 3 days in a clean bench and weighted. The organs were digested in aqua regia by boiling at 130 °C. The reaction was repeated until the solution was transparent, which was diluted with DI water. The fluorescence of the solution was measured, and the concentrations of FNDs and HA–FND conjugates were calculated in comparison with that of the control ($n = 3$).

2.11. Renal clearance

PBS, FNDs, and HA–FND conjugates (100 μL, 10 mg mL^{-1} of total FNDs) were intravenously injected into 6 week female balb/c nude mice (weight ≈ 20 g). Urine was collected for 5 days from metabolic cages. The absorbance of PBS and HA–FND conjugates in mice urine was analysed by UV-vis spectroscopy (JASCO J-715). The fluorescent intensity of PBS, FNDs, and HA–FND
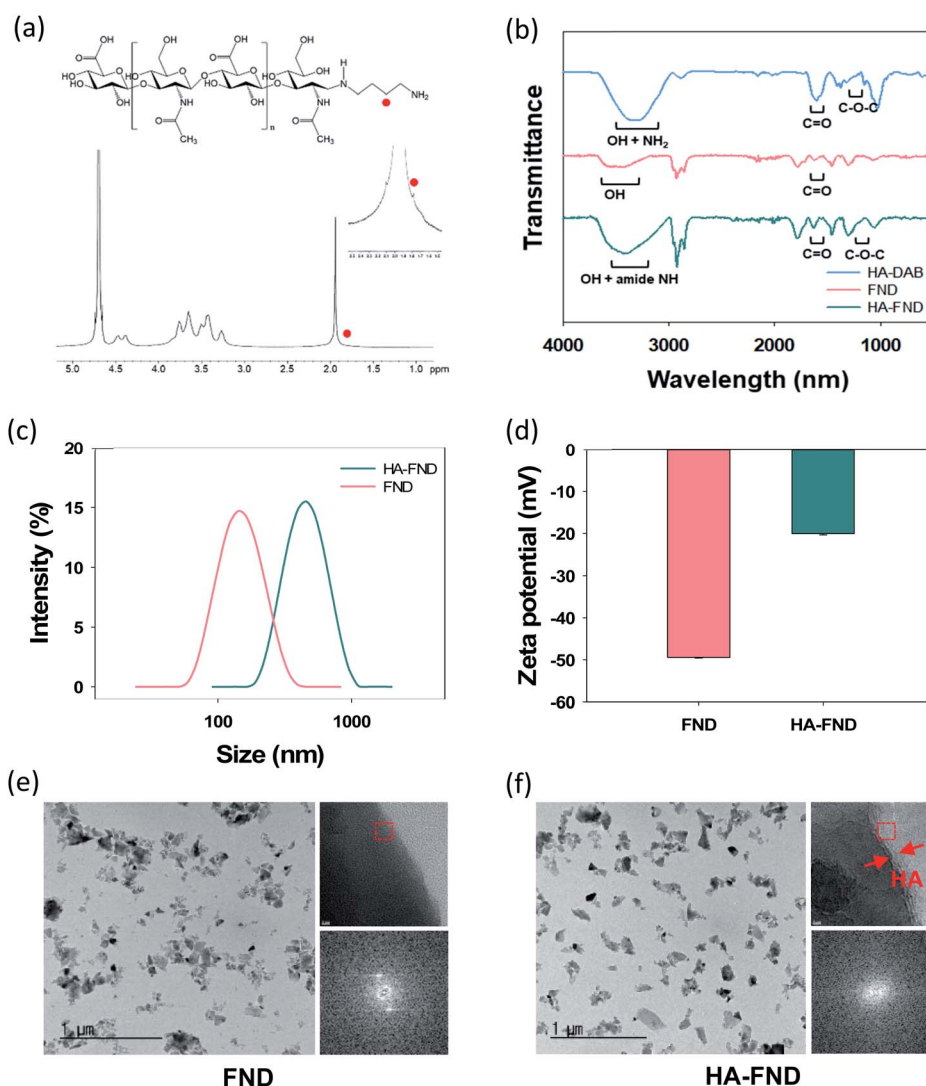

Fig. 2 (a) ^{1}H NMR spectra of DAB modified HA. (b) FT-IR spectra of HA–DAB, FNDs, and HA–FND conjugates. (c) Zeta particle size distribution of FNDs and HA–FND conjugates. (d) Zeta potential of FNDs and HA–FND conjugates. HR-TEM images of (e) FNDs and (f) HA–FND conjugates.

conjugates in mice urine were measured with a microplate fluorometer (Fluoroskan ascent FL, Thermo Scientific).

2.12. Histological analysis

Histological analysis with H&E staining. HA–FND conjugates (100 μL, 10 mg mL^{-1} of total FNDs) were intravenously injected into 6 week female balb/c nude mice (weight ≈ 20 g). The mice were sacrificed and the organs including the liver, heart, lung, kidney, and spleen were collected and fixed in 4% formaldehyde for a day. The organs were analyzed with H&E staining to assess the biocompatibility of HA–FND conjugates.

2.13. Statistical analysis

All data are expressed in means ± standard deviations (SDs). Statistical analysis was performed with an unpaired student's t-test. P values lower than 0.05 were considered statistically significant.

3. Results and discussion

3.1. Characteristics of FNDs and HA–FND conjugates

HA–FND conjugates were synthesized by amide bond formation between the carboxyl group of FNDs and the terminal amine group of HA–DAB via the 1-ethyl-3-(3-dimethylaminopropyl) carbodiimide (EDC) chemistry. The molar ratio of FNDs and HA–DAB was optimized to be 10 : 1 for the carboxyl groups of FNDs and amine groups of HA–DAB in terms of the particle size and its distribution. First, the end group of HA was modified with DAB and the successful synthesis of HA–DAB was confirmed by ^{1}H NMR spectroscopy (Fig. 2a). In ^{1}H NMR spectrum, the terminal amine group peak of HA–DAB was observed around 1.7 ppm. The successful synthesis of HA–DAB and HA–FND conjugates was also confirmed by FT-IR (Fig. 2b). HA–DAB showed C–O–C bending peak (1200–1180 cm^{-1}), amide C=O peak (1750–1700 cm^{-1}), and amine N–H with alcohol O–H peak (3400–3200 cm^{-1}). FNDs showed carboxyl C=O peak (1750–1700 cm^{-1}), and O–H peak (3650–3400 cm^{-1}). The FT-IR spectrum of HA–FND conjugates showed C–O–C bending peak (1200–1180 cm^{-1}), amide C=O peak (1750–1700 cm^{-1}), amide N–H peak (3500–3200 cm^{-1}), and alcohol O–H peak (3600–3200 cm^{-1}), which corroborated the conjugation of HA and FNDs.[17] The particle sizes and zeta potentials of FNDs and HA–FND conjugates were analysed by dynamic light scattering (DLS) (Fig. 2c and d). FNDs appeared to have a particle size of 140 nm and zeta potential of −49 ± 0.17 mV due to the carboxyl groups. HA–FND conjugates had a particle size of 450 nm and zeta potential of −20.07 ± 0.32 mV. HR-TEM images showed the morphology and size of FNDs and HA–FND conjugates, which were well matched with the size data of DLS analysis (Fig. 2e and f).[45] Moreover, HA–FND conjugates were well dispersed in water due to the HA compared to FNDs as shown on HR-TEM images with 50k magnification. In 800k magnification images, while only the crystal lattices of FND were visible, the amorphous coating layer of HA in HA–FND conjugate was also observed on the crystal plane of FND, indicating the successful conjugation of HA on the surface of FND.
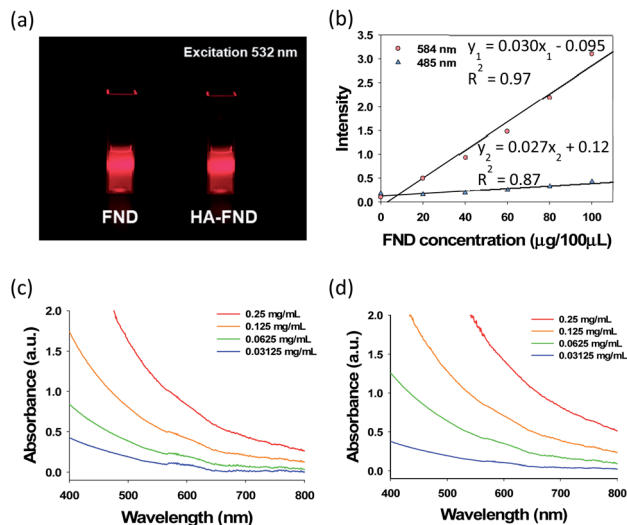

Fig. 3 (a) A photo-image of FNDs and HA–FND conjugates under 532 nm laser irradiation. (b) Fluorescence of FNDs at 485 and 584 nm excitation. UV-vis spectra of (c) FNDs and (d) HA–FND conjugates.

After that, we assessed the optical properties of FNDs and HA–FND conjugates. The fluorescence of FNDs and HA–FND conjugates was analysed at the excitation wavelength of 532 nm with a 600 nm long band filter for the red fluorescence of FNDs (Fig. 3a). In addition, we assessed the fluorescence of FNDs at different excitation and emission wavelengths. As shown in Fig. 3b, the fluorescence increased rapidly with increasing concentration of FNDs at the excitation wavelength of 584 nm and the emission wavelength of 650 nm. The regression line of the graph was linear with the fluorescence intensity of y_1, concentration of FNDs of x, and a coefficient of determination, R_1^2 of 0.97. In contrast, at 485 nm excitation and 538 nm emission wavelength, the fluorescence intensity, y_2, hardly increased and the linearity was weaker with a coefficient of determination, R_2^2 of 0.87. The value of y_1 was used for the quantitative analysis in the following experiments. Since FNDs have a high scattering property with increasing concentration, the absorbance peaks of FNDs (Fig. 3c) and HA–FND conjugates (Fig. 3d) are represented distinctly at the range of 580–620 nm.

3.2. *In vitro* cellular uptake and cell viability test

Confocal microscopy was performed to visualize the cellular uptake of FNDs, HA–FND conjugates, and HA–FND conjugates labelled with fluorescein (FITC) into HepG2 liver cancer cells and FL83b normal liver cells with HA receptors such as CD44. HepG2 cells were incubated with PBS, FNDs, and HA–FND conjugates, respectively. To confirm the target-specific delivery via HA receptor mediated endocytosis, a large amount of free HA was pre-incubated with the cells. As shown in Fig. 4a, the control cells emitted only blue fluorescence of DAPI. Compared to FNDs treated cells, the cells treated with HA–FND conjugates emitted more red fluorescence. In addition, the cells pre-incubated with enough HA showed the reduced red fluorescence compared to the cells treated with HA–FND conjugates,
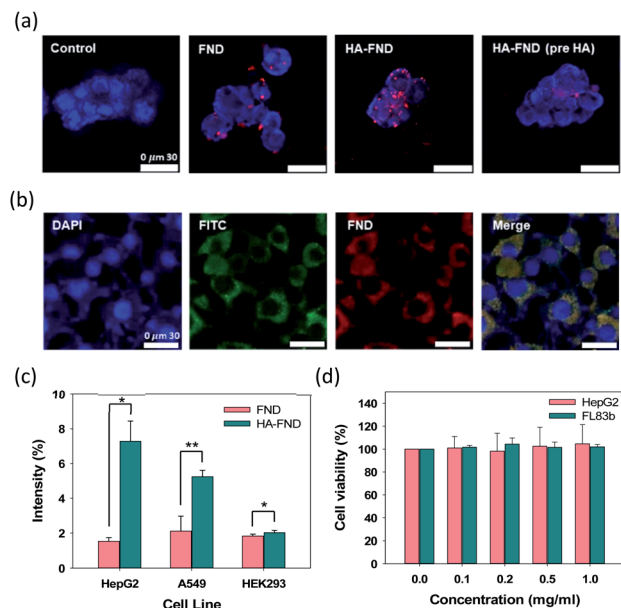
Fig. 4 (a) Confocal microscopic images of HepG2 cells treated with PBS as a control, FNDs, HA–FND conjugates without and with HA preincubation. (b) Confocal microscopic images of FL83b cells treated with HA–FITC-FND conjugates. (c) Fluorescent intensity of FNDs and HA–FND conjugates in HepG2, A549, and HEK293 cells ($n = 3$, *$P \leq$ 0.05 and **$P \leq$ 0.01, FNDs vs. HA–FND conjugates in each cell). (d) Cell viability of HepG2 and FL83b cells after treatment with FNDs and HA–FND conjugates ($n = 3$). Error bars represent standard deviation of three experiments.

location of HA–FITC and the merged image reveals the colocalization of HA–FITC and FNDs. Fig. 4c shows quantitatively the target-specific intracellular delivery of HA–FND conjugates into HepG2, A549 lung cancer cells, and HEK293 kidney cells. After 12 h incubation, cellular uptake of FNDs occurred 1.54 ± 0.20, 2.11 ± 0.87, and 1.83 ± 0.11% and that of HA–FND conjugates were represented 7.28 ± 1.16, 5.24 ± 0.37, and 2.02 ± 0.13% in HepG2, A529, and HEK293 cells, respectively. Because the liver cells have many HA receptors, the highest amount of HA–FND conjugates was uptaken to HepG2 cells compared to other cells. In addition, the fluorescence of HA–FND conjugates was 4.7 times stronger than that of FNDs in HepG2 cells. In contrast, the fluorescence of HA–FND conjugates was 2.48 times stronger than that of FNDs in A549 cells with HA–receptors. However, HEK293 cells without HA receptors showed similar fluorescence intensity for both FNDs and HA–FND conjugates. These results revealed that HA–FND conjugates were well uptaken into the liver cells due to HA receptors.

The biocompatibility of HA–FND conjugates was assessed by measuring the cell viability with cell counting kit-8 (CCK-8) at 7 days post-incubation. HepG2 and FL83b cells were seeded in a 96-well plate and treated with various concentrations of HA–FND conjugates in DMEM (0, 0.1, 0.2, 0.5, and 1 mg mL^{-1}). As shown in Fig. 4d, HA–FND conjugates showed no significant toxicity maintaining the cell viability for up to 7 days. On the basis of these results, we decide to carry out *in vivo* imaging of HA–FND conjugates for the target-specific delivery to the liver tissues with abundant HA receptors.

indicating the HA receptor mediated endocytosis. Fig. 4b shows the confocal microscopic images of FL83b cells incubated with HA–FITC–FND conjugates. The green fluorescence indicates the

3.3. Fluorescence lifetime imaging of HA–FND conjugates

To investigate *in vivo* imaging capability of HA–FND conjugates, we performed fluorescence lifetime (FLT) imaging in live mice.
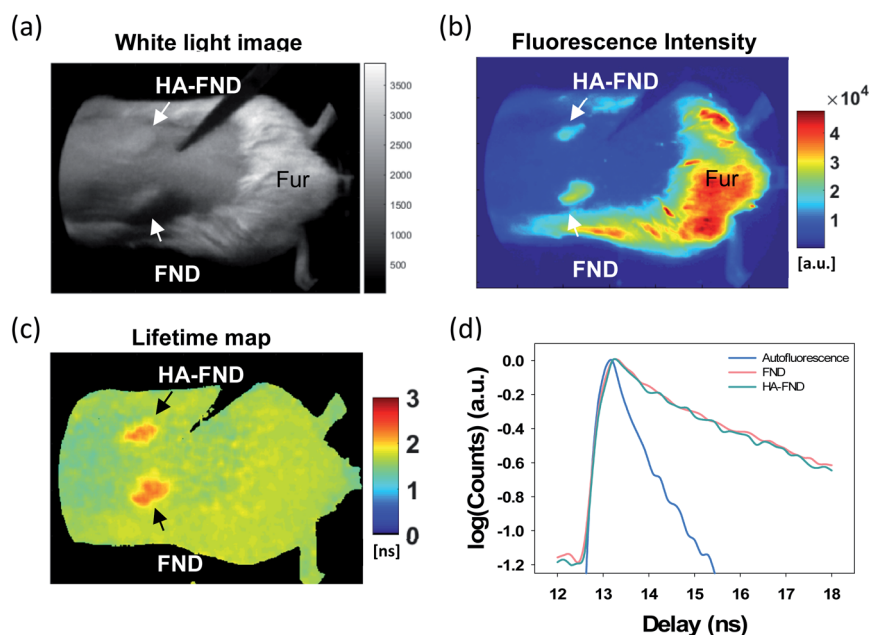

Fig. 5 *In vivo* time-domain imaging of HA–FND conjugates: (a) white light image, (b) color weighted intensity image, and (c) FLT maps obtained by single exponential fits to the decay of time-domain (TD) data. (d) TD fluorescence decay signals of autofluorescence from fur (blue), FNDs (pink), and HA–FND conjugates (green).

The back of mice was shaved, and each 100 μL of FNDs and HA–FND conjugates (20 mg mL^{-1}) was injected subcutaneously onto the shaved skin. The white light image showed the location of the injection site of FNDs and HA–FND conjugates, and the remaining mouse fur (Fig. 5a). The fluorescence signals above 580 nm were collected by using a long pass filter with 540 ± 20 nm excitation (Fig. 5b). On the traditional continuous wave (CW) fluorescence image, the fluorescence of FNDs and HA–FND conjugates was clearly distinguished from the background skin signal, but the mouse fur showed a considerably strong autofluorescence which was indistinguishable from those of FNDs and HA–FND conjugates. On the other hand, FLT maps offered a clear contrast between FNDs/HA–FND conjugates and autofluorescence (Fig. 5c). Fig. 5d shows the single exponential fit of the time-domain (TD) fluorescence decay. The FLT of the FNDs/HA–FND conjugates was calculated to ∼2.3 ns, which was longer than that of the autofluorescence (1.6 ns). These results suggested that the FLT-based bioimaging could enhance the targeted contrast in the presence of a strong autofluorescence.

3.4. *In vivo* molecular imaging for liver targeted delivery

The liver targeting of HA–FND conjugates was observed with IVIS at the excitation wavelength of 605 nm. Generally, laboratory animal diets contain fluorescent materials such as alfalfa, which interfere with *in vivo* imaging fluorophores. To reduce the background signal of mice, we fed purified food to the mice before and during imaging. *In vivo* fluorescence images were obtained and unmixed from auto-fluorescence after intravenous injection of FNDs and HA–FND conjugates for 7 days at time points of 0 h as control, 6 h, 30 h, 54 h, and 168 h. Fig. 6a shows the IVIS images before and after injection of FNDs. After 6 h, the fluorescence was observed in the liver and lung and appeared in the liver mostly after 30 h. Since then, the fluorescence had decreased for 7 days. Fig. 6b shows IVIS images before and after injection of HA–FND conjugates. The fluorescence of HA–FND conjugates was the highest in the liver, whereas that of FNDs was the highest in the lung. The liver emitted little autofluorescence before injection of FNDs and HA–FND conjugates. After injection of HA–FND conjugates, the fluorescence intensity gradually increased to the value of 46.0 ± 3.56 × 10^6 phot per cm^2 per s for up to 30 h and decreased to 2.51 ± 0.704 × 10^6 phot per cm^2 per s in 168 h. In contrast, the average fluorescence intensity after FNDs injection increased to 19.8 ± 2.46 × 10^6 phot per cm^2 per s and decreased to 2.79 ± 0.335 × 10^6 phot per cm^2 per s in 168 h. The increased fluorescence of the liver with HA–FND conjugates was 1.83 times in 6 h and 2.33 times in 30 h higher than that of FNDs.

3.5. *Ex vivo* biodistribution, clearance, and histological analysis with H&E staining

The biodistribution of FNDs and HA–FND conjugates into the major organs was investigated at 6 h and 30 h post-injection. After the sacrifice of the mice, the main organs including the liver, heart, lung, kidney, and spleen were collected and digested in aqua regia. Due to the high chemical stability of FNDs, the unique optical properties might be well preserved compared with organic dyes and fluorescent proteins. As shown in Fig. 7a, 7.76 ± 0.26% of FNDs and 13.6 ± 0.44% of HA–FND conjugates
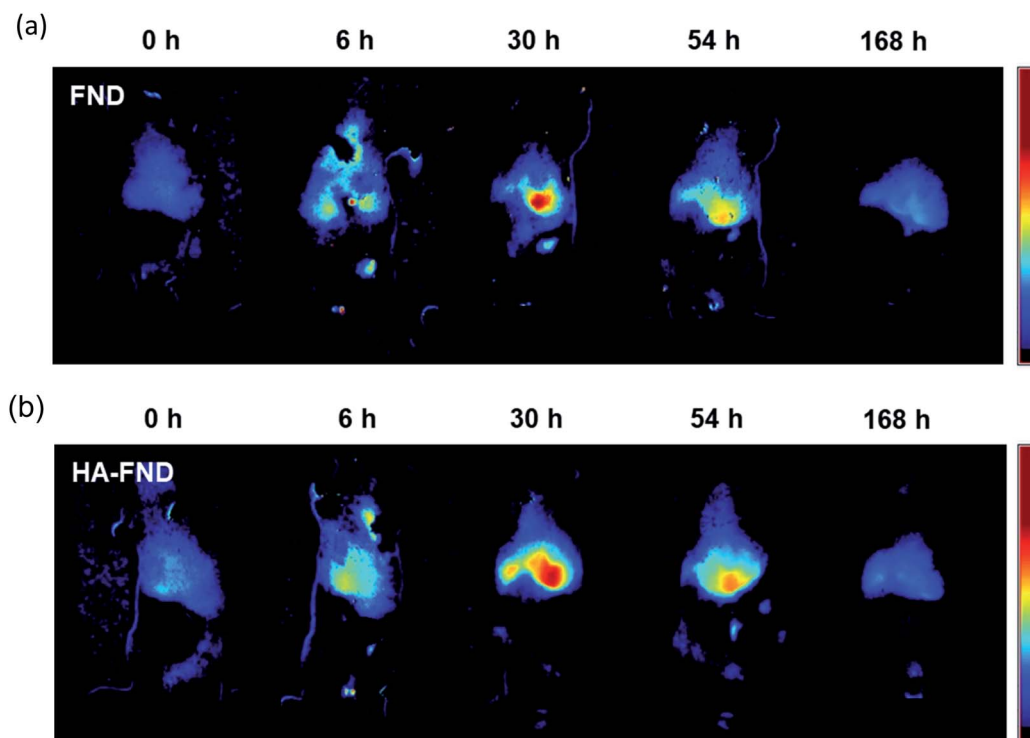

Fig. 6 *In vivo* fluorescence images for liver targeting at 0, 6, 30, 54, and 168 h after intravenous injection of (a) FNDs and (b) HA–FND conjugates.

were observed in the liver and $13.2 \pm 0.52\%$ of FNDs and $7.65 \pm 0.81\%$ of HA–FND conjugates were represented in the lung after 6 h. The amount of HA–FND conjugates was 75.5% higher than that of FNDs in the liver. After 30 h, the amount of FNDs was $11.5 \pm 0.050\%$ and that of HA–FND conjugates in the liver was $22.0 \pm 0.14\%$, which was 91.3% higher than that of FNDs. On the other hand, FNDs and HA–FND conjugates were measured in the lung by 11.0 ± 0.71 and $6.17 \pm 0.13\%$, respectively (Fig. 7b). In accordance with the bioimaging results, the amount of HA–FND conjugates was the highest in the liver, whereas that of FNDs was the highest in the lung. The amount of FNDs and HA–FND conjugates was small but not so much different from each in the heart, kidney, and spleen (FNDs, 0.73, 1.18, and 0.84% after 6 h and 1.26, 1.56, and 2.38% after 30 h; HA–FND, 1.03, 0.11, and 0.35% after 6 h, and 1.30, 0.31, and 1.03% after 30 h). These results confirmed the liver targeted delivery of HA–FND conjugates.

The renal clearance test was performed to assess the accumulation of FNDs and HA–FND conjugates in the body. Fig. 7c shows the absorbance spectra of collected urine after injection of PBS and HA–FND conjugates. HA–FND conjugates were detected in the urine at the range of 580–620 nm. The peak was similar with that in Fig. 3c and d. Additionally, we quantified the urinary excretion for 5 days to assess the renal clearance of FNDs and HA–FND conjugates after intravenous injection. The excreted amount of FNDs and HA–FND conjugates gradually

increased in the urine. FNDs and HA–FND conjugates were removed more than 90% from the body by renal clearance for 5 days, which is consistent with the absence of fluorescence of FNDs and HA–FND conjugates after 168 h in Fig. 6.

Finally, histological analysis with H&E staining was conducted to assess *in vivo* safety of HA–FND conjugates. After intravenous injection of HA–FND conjugates, major organs were collected including the liver, heart, lung, kidney, and spleen in 5 days. There were no inflammation and histological difference between the control group and the HA–FND conjugates treated group (Fig. 7e). These results revealed the safety of HA–FND conjugates as a target-specific molecular imaging agent. Recently, nanodiamonds have been successfully harnessed for high-contrast MR imaging in water at room temperature and ultra-low magnetic field.[46–48] The spin polarization from paramagnetic impurities on the surface of nanodiamonds to ^1H spins in the surrounding water solution appeared to create the MRI contrast. Taken together, HA–FND conjugates would be developed as a promising target-specific multimodal imaging agent for various diagnostic applications.

4. Conclusions

We successfully synthesized and characterized HA–FND conjugates for *in vivo* high contrast fluorescent imaging applications. After confirming the safety of HA–FND conjugates by the cell viability test, we confirmed the target-specific uptake of HA–FND conjugates to the cells with HA receptors *via* HA receptor mediated endocytosis. The FLT imaging revealed the capability of HA–FND conjugates as a fluorescent imaging contrast agent. After intravenous injection of FNDs and HA–FND conjugates, IVIS imaging and biodistribution assessment in the major organs confirmed their statistically significant targeted delivery to the liver. In addition, the renal clearance test and histological analysis with H&E staining revealed *in vivo* safety of HA–FND conjugates. In a word, HA–FND conjugates would be a promising liver targeted imaging contrast agent and applied for various diagnostic and theranostic applications such as multimodal imaging and drug delivery, targeting various HA–receptors in the body.

Conflicts of interest

There are no conflicts to declare.
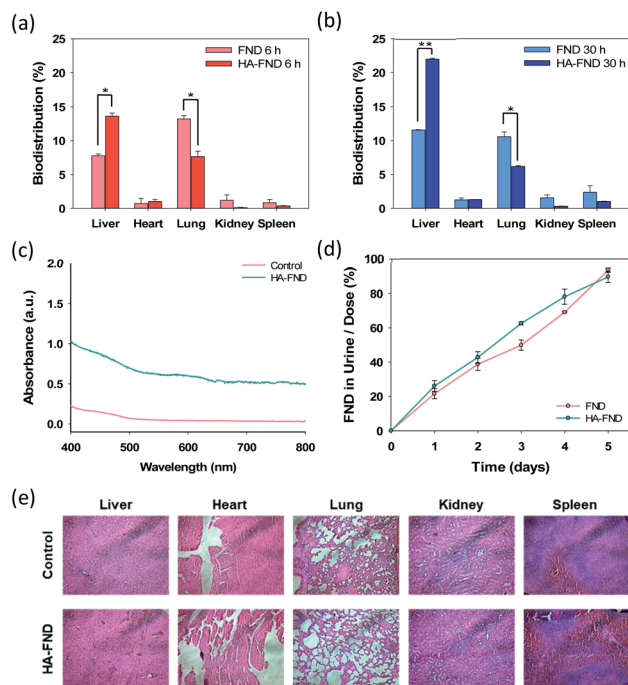
Acknowledgements

Fig. 7 Biodistribution of FNDs and HA–FND conjugates in five different organs at (a) 6 h and (b) 30 h after intravenous injection ($n = 3$). Error bars represent standard deviation of three experiments ($*P \leq 0.05$ and $**P \leq 0.01$, FNDs *vs.* HA–FND conjugates in the liver and lung). (c) The absorbance spectra of urine 48 h after intravenous injection of HA–FND conjugates. (d) Quantitative analysis of renal clearance after intravenous injection of FNDs and HA–FNDs ($n = 3$). (e) Histological analysis with H&E staining of dissected liver, heart, lung, kidney, and spleen after intravenous injection of HA–FND conjugates.

References

1 R. Welssleder and U. Mahmood, *Radiology*, 2001, **219**, 316–333.

2 C. Yu, H. Bao, Z. Chen, X. Li, X. Liu, W. Wang, J. Huang and Z. Zhang, *J. Mater. Chem. B*, 2021, **9**, 2854–2865.

3 D. Lee, S. Beack, J. Yoo, S. K. Kim, C. Lee, W. Kwon, S. K. Hahn and C. Kim, *Adv. Funct. Mater.*, 2018, **28**, 1–9.

4 M. H. Shin, E. Y. Park, S. Han, H. S. Jung, D. H. Keum, G. H. Lee, T. Kim, C. Kim, K. S. Kim, S. H. Yun and S. K. Hahn, *Adv. Healthc. Mater.*, 2019, **8**, 1–11.

5 Q. Li, S. Li, S. He, W. Chen, P. Cheng, Y. Zhang, Q. Miao and K. Pu, *Angew. Chemie*, 2020, **132**, 7084–7089.

6 J. Huang and K. Pu, *Angew. Chemie*, 2020, **132**, 11813–11827.

7 Y. Zhang, S. He, W. Chen, Y. Liu, X. Zhang, Q. Miao and K. Pu, *Angew. Chem., Int. Ed.*, 2021, **60**, 5921–5927.

8 Y. Y. Hui, C. L. Cheng and H. C. Chang, *J. Phys. D. Appl. Phys.*, 2010, **43**, 37.

9 K. D. Wegner and N. Hildebrandt, *Chem. Soc. Rev.*, 2015, **44**, 4792–4834.

10 I. V. Martynenko, A. P. Litvin, F. Purcell-Milton, A. V. Baranov, A. V. Fedorov and Y. K. Gun'Ko, *J. Mater. Chem. B*, 2017, **5**, 6701–6727.

11 M. X. Yu, J. J. Ma, J. M. Wang, W. G. Cai, Z. Zhang, B. Huang, M. Y. Sun, Q. Y. Cheng, Z. L. Zhang, D. W. Pang and Z. Q. Tian, *ACS Appl. Nano Mater.*, 2020, **3**, 6071–6077.

12 S. A. Bansal, V. Kumar, J. Karimi, A. P. Singh and S. Kumar, *Nanoscale Adv*, 2020, **2**, 3764–3787.

13 Z. Yu, H. Xiao, X. Zhang, Y. Yang, Y. Yu, H. Chen, X. Meng, W. Ma, M. Yu, Z. Li, C. Li and H. Liu, *ACS Nano*, 2020, **14**, 13536–13547.

14 Y. Bao, J. A. Sherwood and Z. Sun, *J. Mater. Chem. C*, 2018, **6**, 1280–1290.

15 Y. Yan, J. Chen, Z. Yang, X. Zhang, Z. Liu and J. Hua, *J. Mater. Chem. B*, 2018, **6**, 7420–7426.

16 D. M. Chudakov, M. V. Matz, S. Lukyanov and K. A. Lukyanov, *Physiol. Rev.*, 2010, **90**, 1103–1163.

17 G. Qiao, G. Chen, Q. Wen, W. Liu, J. Gao, Z. Yu and Q. Wang, *J. Colloid Interface Sci.*, 2020, **580**, 88–98.

18 C. J. Weijer, *Science*, 2003, **300**, 96–100.

19 D. Wang, Y. Tong, Y. Li, Z. Tian, R. Cao and B. Yang, *Diam. Relat. Mater.*, 2013, **36**, 26–34.

20 L. J. Su, M. S. Wu, Y. Y. Hui, B. M. Chang, L. Pan, P. C. Hsu, Y. T. Chen, H. N. Ho, Y. H. Huang, T. Y. Ling, H. H. Hsu and H. C. Chang, *Sci. Rep.*, 2017, **7**, 1–11.

21 V. N. Mochalin, O. Shenderova, D. Ho and Y. Gogotsi, *Nat. Nanotechnol.*, 2012, **7**, 11–23.

22 S. J. Yu, M. W. Kang, H. C. Chang, K. M. Chen and Y. C. Yu, *J. Am. Chem. Soc.*, 2005, **127**, 17604–17605.

23 Y. R. Chang, H. Y. Lee, K. Chen, C. C. Chang, D. S. Tsai, C. C. Fu, T. S. Lim, Y. K. Tzeng, C. Y. Fang, C. C. Han, H. C. Chang and W. Fann, *Nat. Nanotechnol.*, 2008, **3**, 284–288.

24 S. Claveau, J. R. Bertrand and F. Treussart, *Micromachines*, 2018, **9**, 1–13.

25 M. F. Weng, S. Y. Chiang, N. S. Wang and H. Niu, *Diam. Relat. Mater.*, 2009, **18**, 587–591.

26 V. Vaijayanthimala, P. Y. Cheng, S. H. Yeh, K. K. Liu, C. H. Hsiao, J. I. Chao and H. C. Chang, *Biomaterials*, 2012, **33**, 7794–7802.

27 C. Desai, K. Chen and S. Mitra, *Environ. Sci. Process. Impacts*, 2014, **16**, 518–523.

28 H. Huang, M. Liu, X. Tuo, J. Chen, L. Mao, Y. Wen, J. Tian, N. Zhou, X. Zhang and Y. Wei, *Appl. Surf. Sci.*, 2018, **439**, 1143–1151.

29 L. Zhao, Y. H. Xu, T. Akasaka, S. Abe, N. Komatsu, F. Watari and X. Chen, *Biomaterials*, 2014, **35**, 5393–5406.

30 W. W. W. Hsiao, Y. Y. Hui, P. C. Tsai and H. C. Chang, *Acc. Chem. Res.*, 2016, **49**, 400–407.

31 W. Liu, B. Naydenov, S. Chakrabortty, B. Wuensch, K. Hubner, S. Ritz, H. Colfen, H. Barth, K. Koynov, H. Qi, R. Leiter, R. Reuter, J. Wrachtrup, F. Boldt, J. Scheuer, U. Kaiser, M. Sison, T. Lasser, P. Tinnefeld, F. Jelezko, P. Walther, Y. Wu and T. Weil, *Nano Lett.*, 2016, **16**, 6236–6244.

32 Z. Y. Lien, T. C. Hsu, K. K. Liu, W. S. Liao, K. C. Hwang and J. I. Chao, *Biomaterials*, 2012, **33**, 6172–6185.

33 V. Vaijayanthimala, P. Y. Cheng, S. H. Yeh, K. K. Liu, C. H. Hsiao, J. I. Chao and H. C. Chang, *Biomaterials*, 2012, **33**, 7794–7802.

34 K. Kakehi, M. Kinoshita and S. I. Yasueda, *J. Chromatogr. B: Anal. Technol. Biomed. Life Sci.*, 2003, **797**, 347–355.

35 J. Necas, L. Bartosikova, P. Brauner and J. Kolar, *Vet. Med.*, 2008, **53**, 397–411.

36 V. N. Khabarov, P. Y. Boykov and M. A. Selyanin, *Vet. Med.*, 2008, **8**, 397–411.

37 H. Kim, H. Jeong, S. Han, S. Beack, B. W. Hwang, M. Shin, S. S. Oh and S. K. Hahn, *Biomaterials*, 2017, **123**, 155–171.

38 E. J. Oh, K. Park, K. S. Kim, J. Kim, J. A. Yang, J. H. Kong, M. Y. Lee, A. S. Hoffman and S. K. Hahn, *J. Control. Release*, 2010, **141**, 2–12.

39 J. H. Sun, Q. Luo, L. L. Liu and G. Bin Song, *World J. Gastroenterol.*, 2016, **22**, 3547–3557.

40 O. Nagano, S. Okazaki and H. Saya, *Oncogene*, 2013, **32**, 5191–5198.

41 H. Lee, J. H. Lee, J. Kim, J. H. Mun, J. Chung, H. Koo, C. Kim, S. H. Yun and S. K. Hahn, *ACS Appl. Mater. Interfaces*, 2016, **8**, 32202–32210.

42 K. Y. Choi, G. Saravanakumar, J. H. Park and K. Park, *Colloids Surfaces B Biointerfaces*, 2012, **99**, 82–94.

43 S. Arpicco, P. Milla, B. Stella and F. Dosio, *Molecules*, 2014, **19**, 3193–3230.

44 B. R. Lin, C. H. Chen, C. H. Chang, S. Kunuku, T. Y. Chen, T. Y. Hsiao, H. K. Yu, Y. J. Chang, L. C. Liao, F. H. Chen, H. Niu and C. P. Lee, *J. Phys. D. Appl. Phys.*, 2019, **52**, 505402.

45 X. Liu, Y. Yang, M. Ling, R. Sun, M. Zhu, J. Chen, M. Yu, Z. Peng, Z. Yu and X. Liu, *Adv. Funct. Mater.*, 2021, **31**, 2101709.

46 W. L. Rice, D. M. Shcherbakova, V. V. Verkhusha and A. T. N. Kumar, *Cancer Res.*, 2015, **75**, 1236–1243.

47 V. P. Bhallamudi and P. C. Hammel, *Nat. Nanotechnol.*, 2015, **10**, 104–106.

48 D. E. J. Waddington, M. Sarracanie, H. Zhang, N. Salameh, D. R. Glenn, E. Rej, T. Gaebel, T. Boele, R. L. Walsworth, D. J. Reilly and M. S. Rosen, *Nat. Commun.*, 2017, **8**, 1–8.